nature communications

Article

https://doi.org/10.1038/s41467-024-51748-1

Molecular basis of inhibition of the amino acid transporter B^0AT1 (SLC6A19)

Received: 9 January 2024

Accepted: 9 August 2024

Published online: 22 August 2024

Check for updates

Junyang Xu[1,4], Ziwei Hu[2,4], Lu Dai[2,4], Aditya Yadav[3,4], Yashan Jiang[3,4], Angelika Bröer[3], Michael G. Gardiner[1], Malcolm McLeod[1], Renhong Yan[2] ✉ & Stefan Bröer[3] ✉

The epithelial neutral amino acid transporter B^0AT1 (SLC6A19) is the major transporter for the absorption of neutral amino acids in the intestine and their reabsorption in the kidney. Mouse models have demonstrated that lack of B^0AT1 can normalize elevated plasma amino acids in rare disorders of amino acid metabolism such as phenylketonuria and urea-cycle disorders, implying a pharmacological approach for their treatment. Here we employ a medicinal chemistry approach to generate B^0AT1 inhibitors with IC_{50}-values of 31-90 nM. High-resolution cryo-EM structures of B^0AT1 in the presence of two compounds from this series identified an allosteric binding site in the vestibule of the transporter. Mechanistically, binding of these inhibitors prevents a movement of TM1 and TM6 that is required for the transporter to make a conformational change from an outward open state to the occluded state.

Amino acid homeostasis is an important factor in cellular and organismal physiology[1]. Plasma amino acid levels are maintained in a narrow range and are used as a diagnostic tool to identify rare diseases, such as phenylketonuria, urea cycle disorders, tyrosinemia, and lysinuric protein intolerance[2]. Smaller deviations of amino acid homeostasis occur in type 2 diabetes and are related to insulin resistance[3,4]. Various strategies are used to treat derangements of amino acid metabolism, such as diet, nitrogen scavengers and supplements[2]. A more recent strategy is to counteract elevated levels of amino acids by decreasing the uptake or increasing the loss of amino acids via inhibition of amino acid transporters. Epithelial amino acid transporters are critical for the absorption of amino acids in the intestine and the reabsorption of amino acids in the kidney[1]. Blockade or lack of these transporters causes reduced absorption in the intestine and loss of amino acids in the kidney[5]. In humans, mutations in the *SLC6A19* gene cause Hartnup disorder, a largely benign condition characterized by aminoaciduria[6]. Consistently, lack of the apical neutral amino acid transporter B^0AT1 (Broad neutral amino acid transporter 1, encoded by the *SLC6A19* gene) has been shown to counteract elevated amino acids in phenylketonuria and urea cycle disorder mouse models[7,8]. Moreover, lack of B^0AT1 has also been shown to improve glucose tolerance through a variety of mechanisms including elevated levels of FGF21, GLP-1[9] and reducing liver triglycerides[10] and may protect against kidney injury[11]. As a result, significant efforts are underway to develop high-affinity selective inhibitors of B^0AT1[10,12–16]. This has been accompanied by the development of a variety of assays to measure B^0AT1 activity, such as proteoliposome flux assay[12], solid supported membrane electrophysiology[16], voltage-sensitive fluorescent dyes (FLIPR)[14,15] and radioactive flux assays in cell lines[14,15].

The amino acid transporter B^0AT1 belongs to the amino acid transporter subfamily of the SLC6 family[17]. This subfamily is characterized by an extended loop linking transmembrane helices 7 and 8. In the case of B^0AT1 this loop is required to form contacts with the single transmembrane helix (TM) proteins collectrin or ACE2, enabling cell surface expression in the kidney[18] and intestine[19], respectively. Mammalian cell lines overexpressing B^0AT1 and collectrin have been employed to characterize inhibitors, but the endogenous transport activity in radioactive uptake assays is substantial, reducing the signal-to-noise ratio[14].

The structure of the B^0AT1/ACE2 complex was recently resolved by single-particle cryo-EM[20]. Despite the significant pharmaceutical interest in B^0AT1 inhibitors, a structural understanding of their binding

[1]Research School of Chemistry, Australian National University, Canberra, ACT, Australia. [2]Department of Biochemistry, Key University Laboratory of Metabolism and Health of Guangdong, School of Medicine, Institute for Biological Electron Microscopy, Southern University of Science and Technology, Shenzhen, Guangdong, China. [3]Research School of Biology, Australian National University, Canberra, ACT, Australia. [4]These authors contributed equally: Junyang Xu, Ziwei Hu, Lu Dai, Aditya Yadav, Yashan Jiang. ✉e-mail: yanrh@sustech.edu.cn; stefan.broeer@anu.edu.au

to the transporter is missing. In contrast, the pharmacology of neurotransmitter transporters of the SLC6 family is well developed. Most neurotransmitter transporter inhibitors act by binding to the orthosteric binding site (S1), but some also bind to an allosteric site in the vestibule of the transporters (S2)[21–24]. Importantly, all serotonin reuptake inhibitors bind with higher affinity to the S1 site than to the S2 site[24].

Initially identified inhibitors of B^0AT1 had IC_{50} values in the 10-100 μM range, such as nimesulide and benztropine[12,14]. Inhibitors derived from high-throughput screening showed IC_{50}-values in the range from 0.4-15 μM, such as cinromide, and compounds CB3, E4 and E18[10,15]. A medicinal chemistry approach based on nimesulide resulted in compound 39 having an IC_{50} of 0.035 μM[13]. The structures of known B^0AT1 inhibitors are shown in Table S1.

In this study we improve the radioactive flux assay by suppressing endogenous transporters and use this improved assay to identify homologues of the recently identified B^0AT1 inhibitor E4 (2-(4-chloro-2,6-dimethylphenoxy)-*N*-propan-2-ylacetamide)[10]. This results in improved compounds with nanomolar affinity. Structural analysis shows binding of these compounds to an allosteric site of the transporter. These results pave the way for rational drug design for an important pharmaceutical target.

Results

Development of an improved B^0AT1 activity assay

To characterize novel inhibitors of B^0AT1 we have used two independent assays, namely a commercial fluorescent plate-reader based assay (FLIPR) and a conventional radioactive uptake assay[14]. While the FLIPR assay is suitable for high-throughput screening, detailed characterization of initial hits requires a secondary assay that directly measures amino acid uptake. Both assays are used in conjunction with a Chinese hamster ovary cell line stably overexpressing B^0AT1 and collectrin (CHO-BC)[14] with L-leucine as a preferred substrate. However, CHO cells also have endogenous transporters for L-leucine[25]. To identify the fraction of L-leucine uptake mediated by B^0AT1, uptake was measured in the presence and absence of Na^+ because B^0AT1 is Na^+-dependent, while the main endogenous L-leucine transporter LAT1 (SLC7A5) is Na^+-independent[14] (Fig. 1a). Two problems arise from endogenous

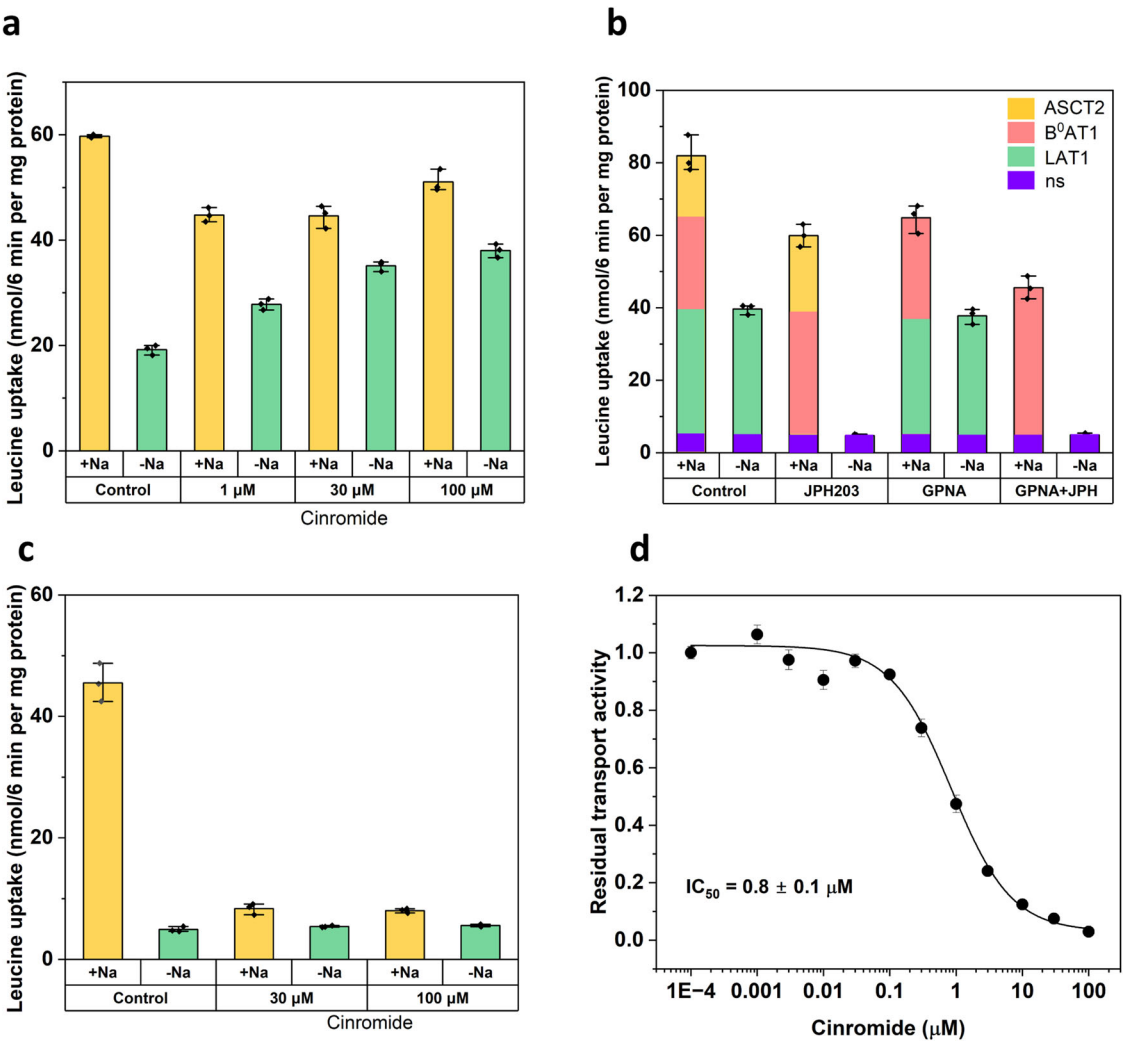

Fig. 1 | Endogenous contributions to leucine transport in the B^0AT1 flux assay. L-leucine transport was characterized in CHO-BC cells using uptake of 150 μM L-[^{14}C]leucine. **a** Uptake of L-leucine was measured in the presence (yellow) and absence (green) of Na^+. An apparent increase of Na^+-independent leucine transport is observed after application of increasing concentrations of B^0AT1 inhibitor cinromide. L-Leucine transport is blocked incompletely due to endogenous transport activities. **b** The Na^+-independent endogenous transport can be blocked by LAT1 inhibitor JPH203. The Na^+-dependent component of L-leucine uptake that is sensitive to inhibition by GPNA (γ-glutamyl-p-nitroanilide) was assigned to ASCT2. The remaining transport activity was assigned to B^0AT1. Transport components are indicated by colour. **c** In the presence of GPNA (3 mM) and JPH203 (3 μM), the remaining Na^+-dependent transport activity is completely blocked by cinromide. (**d**) IC_{50} of cinromide as determined with the optimized assay. All data shown as mean ± SD, individual datapoints were overlayed in all bar graphs (n = 3, n referring to individually seeded cell culture dishes used for each condition or concentration).

amino acid transport when characterizing B^0AT1 inhibitors. First, inhibition can remain incomplete, even when Na^+-independent transport via LAT1 is subtracted, due to the activity of other transporters. Secondly, inhibition of B^0AT1 can result in an apparent increase of Na^+-independent transport activity (LAT1), instead of an expected inhibition of Na^+-dependent L-leucine transport (B^0AT1) (Fig. 1a). The net uptake activity is reduced but for an optimal assay it would be better to isolate the B^0AT1 component. L-leucine uptake in CHO-BC cells is comprised of five components, namely B^0AT1, LAT1 (SLC7A5), ASCT2 (SLC1A5) and SNAT2 (SLC38A2)[26,27] (Fig. 1b). However, SNAT2 activity can be suppressed by a recent change of media[28].

As a first step to improve the assay, we added JPH203 (3 μM), a high-affinity LAT1 inhibitor that blocks Na^+-independent L-leucine transport without affecting B^0AT1[29] (Fig. 1b). The activity of ASCT2 could be suppressed by γ-glutamyl-p-nitroanilide (GPNA, 3 mM)[30]. When both inhibitors were combined, the known B^0AT1 inhibitor cinromide completely blocked the remaining transport activity without increasing Na^+-independent transport (Fig. 1c). Using this optimized assay, we determined an IC_{50} value of 0.8 ± 0.1 μM for cinromide (Fig. 1d), which agrees with earlier measurements[10,15]. An additional advantage of the optimized assay is the reduction of samples, because measurements can be performed in the presence of Na^+ without the need to subtract endogenous transport activity in Na^+-free buffer.

Identification of high-affinity inhibitors of B^0AT1

In a previous high-throughput screen we identified compound E4 (2-(4-chloro-2,6-dimethylphenoxy)-*N*-isopropylacetamide) as a high-affinity inhibitor of B^0AT1[10] with an IC_{50} = 7.7 ± 1.9 μM. When we synthesized a new batch of the compound, we noticed that the inhibitory activity was strongly reduced such that an IC_{50} could not be determined (8% inhibition at 30 μM) (Fig. S1). Subsequent structural characterisation of the original and new batch revealed that the active compound was in fact (2-(4-chloro-3,5-dimethylphenoxy)-*N*-isopropylacetamide). We called this compound JX98 (Fig. 2) and refer to E4 as JX8 to avoid confusion and use these numbers from hereon. This revealed a strong structure-activity relationship (SAR), namely that the methyl-groups of the phenoxy moiety cannot be in the ortho-position but must be in meta-position (Figs. 2 and S1 (JX8 vs. JX98)). Even a single methyl-group in this position reduces the inhibitory potential to a similar extent (JX42). As a result, we performed all subsequent SAR experiments with JX98.

The systematic variation of the JX98 pharmacophore is summarized in Fig. 2 with more detailed information presented in Table S1. Different compound series investigated variation to the aromatic ring substituents, amide substituents, linking heteroatom, and bioisosteres of the amide functional group. Changes to the aromatic ring included the addition or removal of halogen and methyl substituents, and the introduction of several larger ring systems, with the outcome that the larger halogens and a single methyl group led to improved activity (JX174 and JX175). Changes to the amide substitution included exploring longer sidechains, including the introduction of aromatic and polar substituents, with the outcome that linear or branched two and three carbon chains were preferred (JX109 and JX110). Replacing the oxygen linking heteroatom with nitrogen provided analogues with improved activity (JX184). Notably, the secondary amide of the sidechain was essential for inhibitory action and could not be replaced by an ester (JX127), thioester (JX128), *N*-methylated tertiary amide (JX129) or ketone (JX130) (Fig. 2 and Table S1). This suggests that a hydrogen bond donor may be required at this position. The X-ray crystal structure of JX98 (CCDC-2300201, Figure S2a) revealed intramolecular hydrogen bonding between the amide nitrogen and the phenolic ether[31], while the structure of JX225 (CCDC-2300200, Figure S2b) revealed intermolecular hydrogen bonding between the amide N-H and carbonyl of adjacent molecules, highlighting the potential of this secondary amide to mediate intramolecular or intermolecular contacts.

A final series of new compounds (JX225-228 and JX235-240) was generated through combining beneficial changes identified in the systematic investigations described above. These yielded potent inhibitors with IC_{50}-values ranging from 31 nM to 90 nM as measured using the FLIPR assay (Fig. 3). The corresponding IC_{50}-values measured by radioactive uptake were higher, ranging from 111 nM to 440 nM.

High-resolution cryo-EM structures of B^0AT1 in the presence of inhibitors

To understand the mechanism of inhibition further, we determined the structure of B^0AT1 in the presence of JX98 and JX225. The structures of ACE2-B^0AT1 incubated with JX98 and JX225 were resolved at a remarkable resolution of up to 3.18 Å or 3.12 Å, respectively (Figs. 4a and S3–4 and Table S2). Detailed information regarding cryo-EM sample preparation, data collection, processing, and model construction can be found in the "Materials and Methods" section. Electron density maps for selected transmembrane helices are shown in Fig. S5.

In the cryo-EM structures of B^0AT1 incubated with JX98 and JX225, an extra density was found in the vestibule of the transporters when compared with the apo state of B^0AT1 (PDB: 6M18). This pocket is enclosed by TM1b, TM7, TM8 and EL_{7-8}, which is different from the orthosteric substrate binding site enclosed by the unwound region of TM1 and TM6 (Figs. 4b–c and S6). The high-resolution inhibitor-bound structures enabled model building of JX98 and JX225 molecules, which are both enclosed by a series of hydrophobic residues (Figs. 4d–g and S6). As shown in Fig. 4, the poses of JX225 and JX98 exhibit remarkable similarity, as both occupy nearly identical positions within the same binding locale of B^0AT1. Consistent with the analysis of structure-activity relationships, the backbone nitrogen of Trp56 on TM1 has the potential to form hydrogen bonds with the carbonyl oxygen atoms of JX225 and JX98, respectively (Fig. 4d, f), but there was no hydrogen bond to the secondary amine. The halogen atoms of both, JX225 and JX98 exert substantial binding forces, albeit through distinct mechanisms. Through model building, it was discerned that the bromine atom of JX225 has the capability to establish a non-covalent halogen bond[32] with Met423 on TM8, although the angle is not optimal. This interaction may contribute to the increased affinity between JX225 and B^0AT1[33]. In contrast, the chlorine atom of JX98 is located at a greater distance from Met423 and engages in hydrophobic interactions with Val321 and Leu234 on TM7. This difference might be caused by the steric hindrance of methyl groups adjacent to the chlorine atom of JX98. The aromatic rings of both JX225 and JX98 exert strong hydrophobic interaction with B^0AT1 including a series of residues (Fig. 4e–g). The hydrophobic environment surrounding JX225 comprises amino acids Pro59, Ile132, Leu136, Leu234, Val317, Val321, Phe403, and Phe420. The hydrophobic environment surrounding JX98 is primarily mediated by residues Val55, Pro59, Val317, Leu398, Phe400, Phe403, Phe420, Leu 424 and Leu427 (Fig. S6). The different hydrophobic interaction patterns for JX98 and JX225 may also explain their different binding affinities for B^0AT1.

Importantly, the JX98 and JX225 binding site is not located at the traditional S1 substrate binding site of LeuT-fold transporters, but rather overlaps with the S2 allosteric binding site identified in several neurotransmitter transporters in this family[24]. Aligning the JX98 and JX225 bound structures with the apo state of B^0AT1, reveals that the gating residue Phe277 is adopting a more outward open state (Fig. 5a, b). In addition, the engagement of the hydrophobic tails of JX98 and JX225 dislocates the side chain of Trp56, which may prevent a movement of TM1b and TM6a of B^0AT1 that is required for the transporter to make a conformational change from an outward open state to the occluded state (Fig. 5a, b). This can be illustrated by overlaying the inward-open apo structure of the closely related transporter ACE2-

https://doi.org/10.1038/s41467-024-51748-1

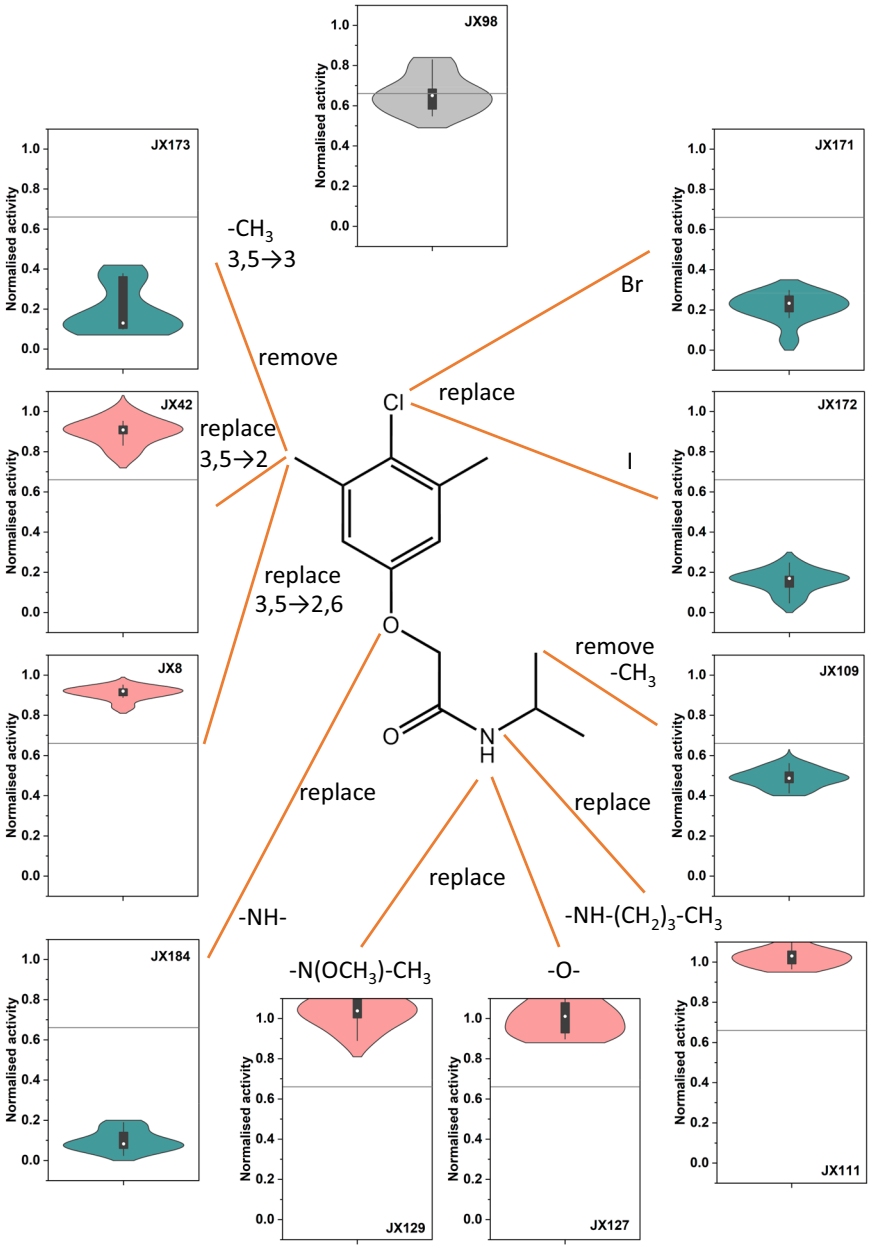

Fig. 2 | Structure-activity relationships of SLC6A19 inhibitor JX98. For each chemical modification the remaining transport activity (measured at 150 μM L-leucine) in the presence of 30 μM inhibitor is shown as a violin plot (n = 10, referring to individually seeded wells) with median (white dot), SD (whiskers), minimum and maximum (violin body) indicated. Better inhibitors result in lower residual activity. Green violins represent improvements, red violins undesirable modifications. Uninhibited cells and inhibition by 30 μM cinromide served as controls for the experiments. More details can be found in Table S1.

SIT1(SLC6A20) (Fig. S7), which has the sidechain of the analogous residue Trp29 penetrating the space occupied by JX98 and JX225. Moreover Phe250 (analogous to Phe277 in B^0AT1) adopts a more inward open conformation[34].

In summary, this study makes three distinct advances in the generation of selective and potent inhibitors of the pharmaceutical target B^0AT1. First, an improved assay for characterization of inhibitors was developed, secondly, a high-affinity allosteric inhibitor of B^0AT1 was generated, and thirdly, an allosteric inhibitory binding site was identified in the vestibule of B^0AT1.

Discussion

The first clinical trials with B^0AT1 inhibitors for the treatment of phenylketonuria have been initiated (NCT05781399) after posting promising preclinical data[35]. This demonstrates B^0AT1 as a validated target for the treatment of orphan diseases with an overabundance of neutral amino acids. This could include orphan diseases such as alkaptonuria, urea cycle disorders and disorders of branched-chain amino acid metabolism. It also demonstrates that small molecule inhibitors of B^0AT1 can be bioavailable and reach plasma concentrations sufficient to inhibit renal reabsorption[35]. Modelling of renal tubular transport[36] suggests that inhibition of >80% is required to reach clinically safe plasma phenylalanine concentrations. JX98 and JX225 have structural similarity to cinromide for which bioavailability has been demonstrated[37]. As a result, a better understanding of potential drug binding sites in members of the SLC6 amino acid transporter subfamily is important. In contrast to drugs that block serotonin, dopamine and noradrenaline transporters, which typically

https://doi.org/10.1038/s41467-024-51748-1

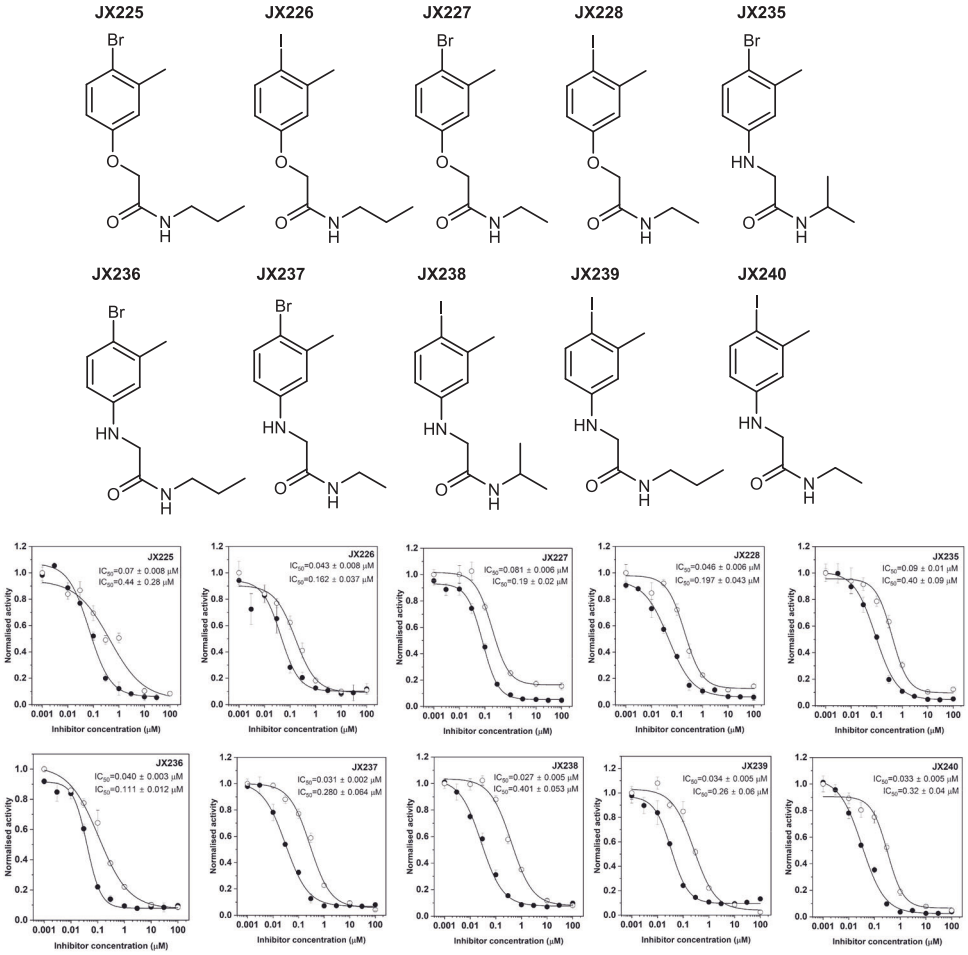

Fig. 3 | Pharmacological properties of optimized B^{0}AT1 inhibitors. Structures of the optimized inhibitors are shown above. L-Leucine transport activity was determined by FLIPR assay (closed symbols) and by radioactive L-leucine uptake assay (open symbols) in CHO-BC cells at the indicated inhibitor concentrations (n = 6, n referring to individually seeded cell culture dishes or wells). Data are shown as mean ± SD. Uninhibited cells and inhibition by 30 μM cinromide served as controls for the experiments.

bind to the orthosteric S1 site[23], JX98 and JX225 bind exclusively to the allosteric site. This is likely the result of the screening strategy employed to isolate the original lead compound E4 (JX98), which made use of an elevated concentration (1.5 mM) of the substrate L-isoleucine against 10 μM inhibitor[10]. This generates a significant competitive pressure excluding compounds that preferentially bind to the S1 site. Citalopram, which has been shown to bind to the S2 site in serotonin transporter SERT, still binds with 1000-fold higher affinity to the S1 site[38]. Only recently has a preferential allosteric inhibitor for SERT being identified from a selection of citalopram analogues[39]. Assignment to the S2 site of SERT was based on displacement experiments with labelled imipramine and citalopram. Here we provide direct structural evidence for selective binding to an allosteric site in B^{0}AT1. While initial docking studies suggested that JX98 could bind to the S1 site[10], we were not able to find structures with an inhibitor bound to this site. The proposed binding pose at the allosteric site does not provide a hydrogen bond to the secondary amine, a feature we would have expected from the SAR. As a result, we cannot exclude that the inhibitor may also bind to the S1 site, where a hydrogen-bond could be formed. Notably, JX225 is structurally similar to the established B^{0}AT1 inhibitor cinromide[15]. Our results therefore suggest a similar binding mode for this compound.

The structure of the LeuT-fold amino acid:sodium symporter MhsT has been determined in an inward-facing conformation[40]. In this structure the vestibule is collapsed, with Trp33, which is homologous to Trp56 in B^{0}AT1, tightly packed by residues from extracellular loop 4, TM3 and TM10. Using docking and mutational studies the experiments suggested that MhsT, like SERT, has a second substrate binding site (S2). The authors propose that binding of the substrate amino acid L-tryptophan to this site can occur when the sidechain of Trp33 rotates out of the way. They further propose that allosteric binding of L-tryptophan could act as a "symport-effector", facilitating the conformational change of the transporter. This S2 binding site is similar to the JX98 and JX225 binding pocket in B^{0}AT1. However, in B^{0}AT1 the allosteric binding site is unambiguously inhibitory. It appears likely that binding of JX98 and JX225 to this site prevents closing of the vestibule and the tight packing of amino acid sidechains, which are required for the transition to the inward-facing conformation. We were unable to generate a structure with inhibitor and substrate bound at the same time. This also explains the largely competitive-type of inhibition exerted by JX98[10]. In B^{0}AT1 the sidechain of Trp56 could act as a pseudo-substrate symport-effector. Notably, L-tryptophan is a poor substrate of B^{0}AT1 with a V_{max} that is 10% of that of the preferred substrate L-methionine[14], which binds to the S1 site[41]. Thus, L-tryptophan could displace the sidechain of Trp56, thereby slowing down the transporter by binding as an allosteric inhibitor. Substrates that prefer the S1 site are fast substrates because they do not compete with the sidechain of Trp56.

Overall, our strategy provides a rational path for the design, development, and in vitro characterisation of allosteric inhibitors

https://doi.org/10.1038/s41467-024-51748-1

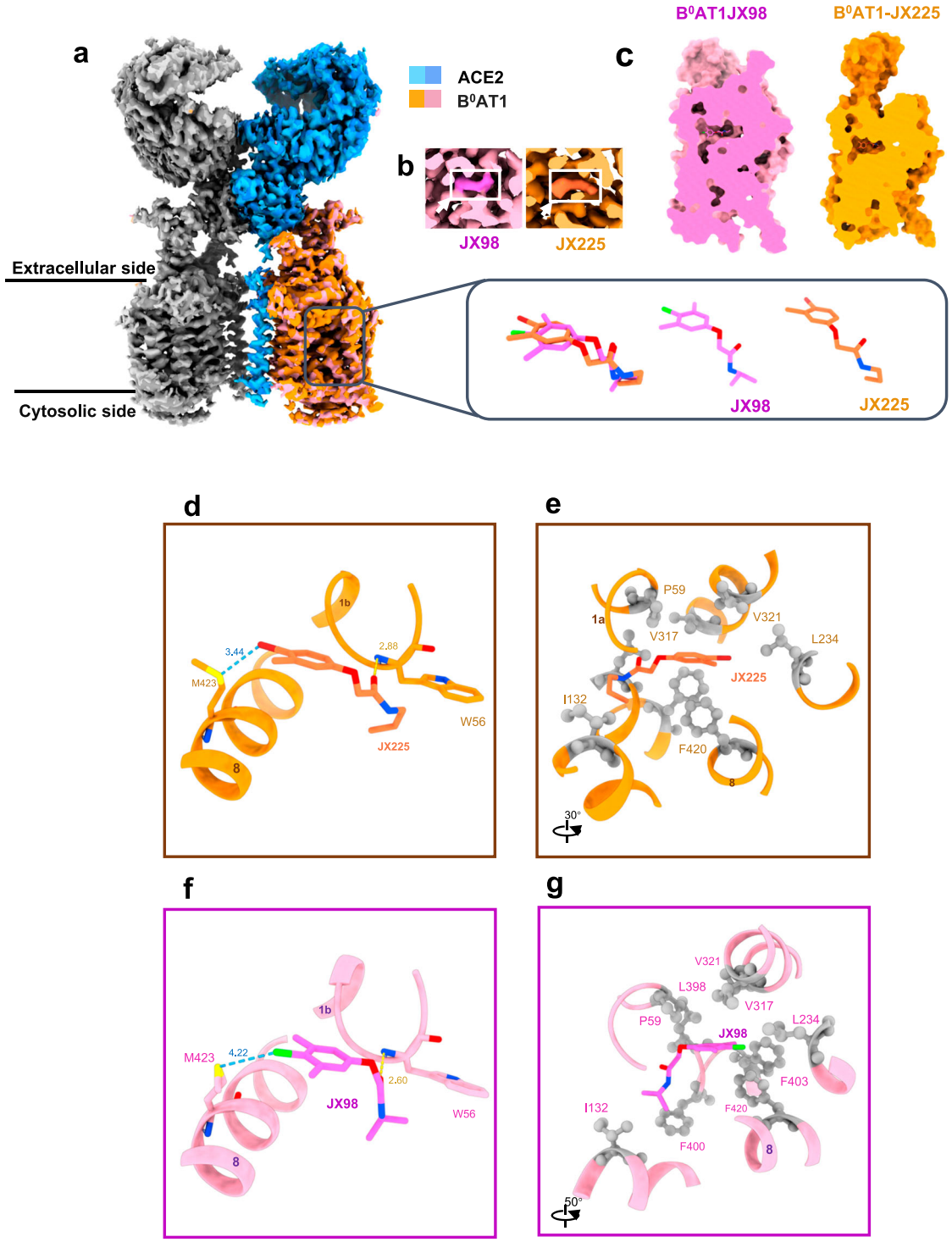

Fig. 4 | Overall structure of the ACE2-B^{0}AT1 bound with inhibitors. a Cryo-EM map of the full length ACE2-B^{0}AT1 heterodimer in complex with inhibitors. ACE2 and B^{0}AT1 bound with JX225 (coral) are represented in sky blue and orange, respectively, while ACE2 and B^{0}AT1 bound with JX98 (magenta) are shown in darker blue and pink, respectively. The structural comparison of JX225 and JX98 is presented in the box. **b** The inserts of the cryo-EM map of the human ACE2-B^{0}AT1 complex show the density corresponding to JX98 and JX225 color-coded in magenta and coral, respectively. **c** Positioning of JX98 and JX225 in the ACE2-B^{0}AT1 complex. Both JX98 and JX225 are centrally located within the presumed transport pathway. **d**, **e** The binding mode of JX225 in B^{0}AT1 is shown, highlighting hydrogen, halogen and hydrophobic interactions. **f**, **g** The binding mode of JX98 in B^{0}AT1 is presented, with schematic diagrams illustrating the interaction environment, following the same representation as in (**d**, **e**).

targeting amino acid transporters in the SLC6 family with potential applications for the treatment of various pathologies. Moreover, we provide insight into the role of the allosteric site in the transport mechanism of SLC6 amino acid transporters.

Methods

The research for this study was carried in accordance with legal requirements for laboratory safety (PC2 Cert-3270), and the office of gene technology regulator (Project 8.18).

https://doi.org/10.1038/s41467-024-51748-1

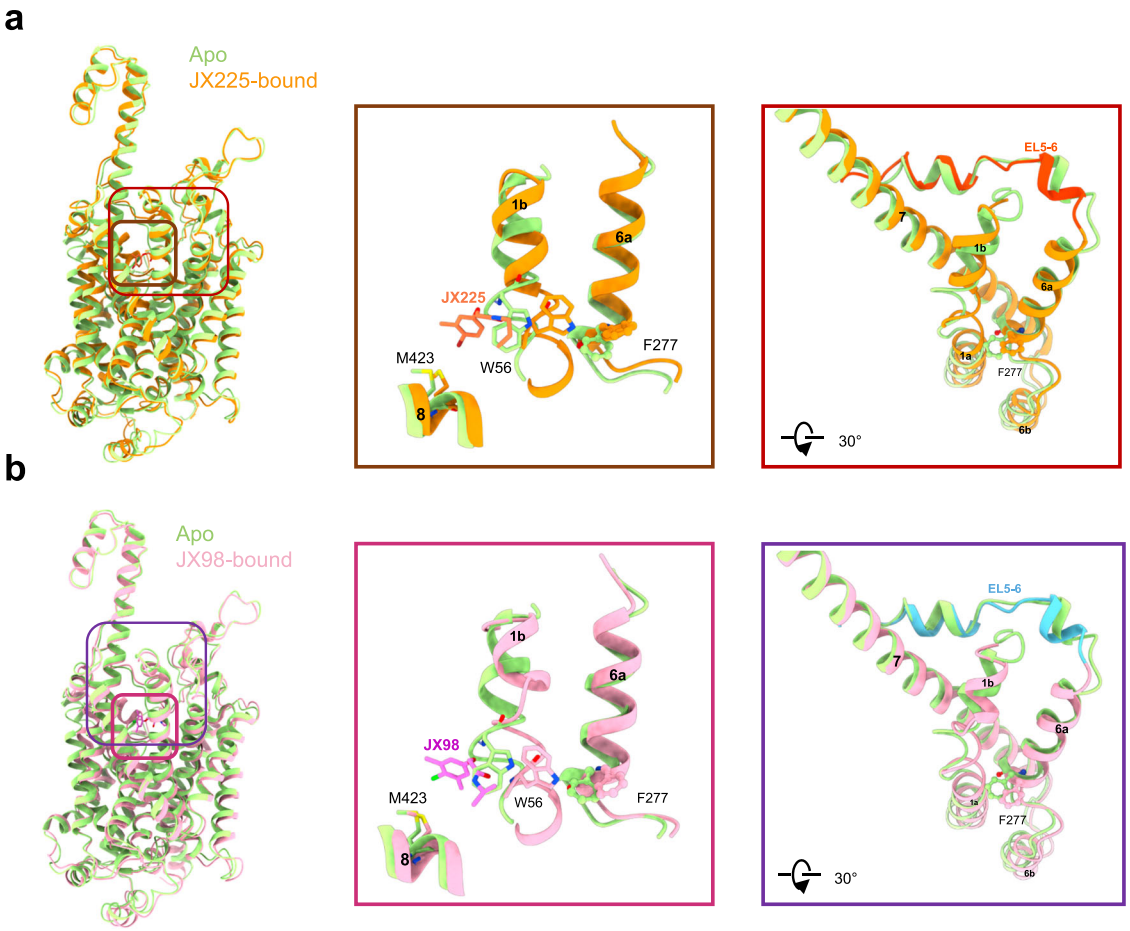

Fig. 5 | The movement of TM1 and TM6 and the role Trp56. A comparison is drawn between the apo structure of B^0AT1 (PDB: 6M18) when bound with JX225 (**a**) and JX98 (**b**), respectively. The apo structure of B^0AT1 is shown in green, while the ligand-bound structures are shown in orange (JX225) and pink (JX98). The alterations in the positions of TM1 and TM6 are depicted in the middle and right panels. JX225 (**a**) and JX98 (**b**) are represented in coral and magenta, respectively.

Materials

The original compound E4[10] was obtained from Enamine (Catalog ID T5320580). The displayed structure is that of (2-(4-chloro-2,6-dimethylphenoxy)-*N*-isopropylacetamide), which is inactive as an inhibitor, but was evaluated in the high throughput screen with an IC_{50} of 2.9 μM. Subsequent structural analysis showed that the compound was in fact (2-(4-chloro-3,5-dimethylphenoxy)-*N*-isopropylacetamide).

All other chemicals were purchased from Merck Millipore.

Protein expression and purification

The full-length human *SLC6A19* (B^0AT1) (GenBank: NM_001003841) was inserted into the pCAG vector (Invitrogen) featuring an N-terminal FLAG tag, while the complete ACE2 sequence was integrated into the pCAG vector (Invitrogen) with 8× His tag. To ensure high transfection efficiency, all plasmids employed for cell transfection underwent preparation using the GoldHi Endo Free Plasmid Maxi Kit (CWBIO).

The recombinant protein was produced through overexpression in HEK293F mammalian cells at 37 °C within a Multitron-Pro shaker (Infors), maintaining a consistent speed of 130 rpm and an environment of 5% CO_2. To achieve co-expression of B^0AT1 and ACE2, cells underwent transient transfection using the plasmids and polyethylenimines (PEIs) (YEASEN). This transfection occurred when the cell density reached approximately 2.0×10^6/mL. For the transfection of one liter of cell culture, around 0.75 mg of B^0AT1 plasmids and 0.75 mg of ACE2 plasmids were carefully pre-mixed with 3 mg of PEIs in 50 mL of fresh medium, allowing them to interact for 15 minutes before being introduced into the cell culture. After the completion of 60 hours of transfection, cells were collected by subjecting them to centrifugation at 3500×g for a duration of 15 minutes. Subsequently, they were gently resuspended in a buffer comprising 25 mM HEPES (pH 7.5), 150 mM NaCl, and a combination of three protease inhibitors: aprotinin (1.3 μg/mL, AMRESCO), pepstatin (0.7 μg/mL, AMRESCO), and leupeptin (5 μg/mL, AMRESCO).

The extraction and purification of the ACE2-B^0AT1 complex were carried out following established methods. First, the membrane fraction was solubilized at 4 °C for 2 hours using 1% (w/v) N-Dodecyl-β-D-maltoside (DDM). Subsequently, cell debris was removed via centrifugation at 15,000 × g for 45 minutes. The resulting supernatant was then applied to anti-FLAG M2 affinity resin (Genscript). Following this step, the resin was thoroughly rinsed with a wash buffer that consisted of 25 mM HEPES (pH 7.5), 150 mM NaCl, and 0.02% (w/v) Glycodiosgenin (GDN). The protein of interest was subsequently eluted using the wash buffer supplemented with 0.2 mg/mL FLAG peptide. The elution was then concentrated and subjected to size-exclusion chromatography using a Superose 6 Increase 10/300 GL column from GE Healthcare. This chromatography was performed in a buffer containing 25 mM Hepes (pH 7.5), 150 mM NaCl, and 0.02% GDN. Finally, the peak fractions were collected and concentrated in preparation for electron microscopy (EM) analysis.

Cryo-EM sample preparation and data acquisition

The purified ACE2-B^0AT1 complex was concentrated to ~ 8 mg/mL and incubated with 200 μM of JX225 or 500 μM JX98 for 0.5 h, before being applied to the grids. Small aliquots (3.3 μL) of the protein complex were

carefully deposited onto glow-discharged holey carbon grids (Quantifoil Au R1.2/1.3). These grids underwent blotting for either 3 seconds or 3.5 seconds and were promptly frozen in liquid ethane, maintained at cryogenic temperatures by liquid nitrogen, utilizing a Vitrobot (Mark IV, Thermo Fisher Scientific). The cryo-EM samples were subsequently transferred to a Titan Krios electron microscope operating at 300 kV. This advanced microscope was equipped with a Gatan K3 detector and a GIF Quantum energy filter. Movie stacks were autonomously acquired using AutoEMation, with an energy filter slit width set at 20 eV. Defocus levels ranged from −1.4 µm to −1.8 µm in super-resolution mode, all under a nominal magnification of 81,000×. Each stack was exposed for 2.998 seconds, with an exposure time of 0.094 seconds per frame, accumulating a total of 32 frames per stack. The total dose rate applied was approximately 50 electrons per Ångström squared (e-/Å2) for each stack. Subsequently, the stacks underwent motion correction using MotionCor2, were binned 2-fold, resulting in a pixel size of 1.095 Å/pixel. Dose weighting was also carried out, and the defocus values were accurately estimated using Gctf[42].

Data processing

Particle selection from the micrographs was performed automatically using the blob picking and template picking process in CryoSPARC v4.4.1[43–47]. Following a round of 2D classification, a subset of high-quality particles was chosen for further processing, advancing into 3D reconstruction via Ab-initio Reconstruction to achieve an initial coarse resolution of the complex. For refinement to attain high resolution, the Heterogeneous Refinement method was employed. During this process, the resolution was continually displayed, assessed through Fourier Shell Correlation, and other diagnostic information provided for each iteration. To further enhance the map quality, particularly in the transmembrane (TM) region, non-uniform refinement and local refinement strategies were implemented. These involved applying appropriate masks to specifically target and improve the resolution in the TM region. The resolution was estimated with the gold-standard Fourier shell correlation 0.143 criterion[48]. Refer to Supplementary Fig. S3 and Table S2 for details of data collection and processing.

Model building and structure refinement

The atomic models of the ACE2-B^{0}AT1 complex, bound with inhibitors, were constructed based on the corresponding Cryo-EM maps, utilizing the previous structure of the ACE2-B^{0}AT1 complex (PDB ID: 6M18) as a template. These models were further manually refined using Coot (v0.9.8.1)[49], with meticulous attention paid to the chemical properties of each residue during the building process.

For precise refinement, structural real-space refinement was conducted employing Phenix (v1.20.1-4487)[50]. Secondary structure and geometry restraints were incorporated into the refinement process to prevent potential overfitting of the structure. To assess the model's performance and potential overfitting, refinement was initially carried out against one of the two independent half maps, following the gold-standard 3D refinement approach. Subsequently, the refined model was rigorously tested against the other half map. Comprehensive statistics related to data collection, 3D reconstruction, and model refinement can be found in Table S2.

Cell lines and media

Recombinant CHO-B^{0}AT1-collectrin Cells (CHO-BC) were generated as described recently[14]. The cell line was derived from the Flp-In™-CHO Cell Line (ThermoFischer Scientific R75807). The cell line was used as provided by the manufacturer. Expression levels of B^{0}AT1 in CHO-BC cells decline over time. As a result, passages <10 were used for experiments. The cells were maintained in Ham's F-12 Glutamax media with 10% (v/v) fetal bovine serum (FBS, Heat inactivated, 10082147 Gibco), 1 mM glutamine, 300 µg/ml hygromycin B and 275 µg/ml geneticin.

Transport assay using FLIPR

Membrane depolarisation induced by amino acid transport was monitored using a FLIPR® kit (Molecular Devices, R8042 BLUE DYE). Before the assay, CHO-BC cells were seeded out at a density of 60,000 cells/well and maintained in a transparent flat bottom 96-well plate (Corning) overnight. After washing three times with Hank's balanced salt solution (136.6 mM NaCl, 5.4 mM KCl, 0.44 mM KH_2PO_4, 2.7 mM Na_2HPO_4, 1.26 mM $CaCl_2$, 0.5 mM $MgCl_2$, 0.4 mM $MgSO_4$, 10 mM HEPES, pH 7.5, supplemented with 5 mM glucose, abbreviated HBSS + G), cells in each well were incubated for 30 minutes at room temperature in 50 µl of HBSS + G pH 7.5 and compounds as indicated, together with 50 µl of dye-loading buffer provided with the kit. Subsequently, the fluorescence signal was detected every 10 s before and after the addition of leucine at a final concentration of 1.5 mM. Fluorescence was detected at room temperature using a PerkinElmer multimode Plate Reader, with an excitation wavelength of 530 nm and emission wavelength of 565 nm.

Transport assay using radiolabelled amino acids

CHO-BC cells with passage numbers from 3 to 10 were used in radiolabelled uptake assays. Before the assay, the cells were seeded out in 35 mm dishes (Corning) and maintained for 48-72 hours until reaching 80-90% confluence. To initiate transport, the culture medium was removed, and the cells were washed three times with HBSS + G pH 7.5. Subsequently, cells were incubated with HBSS + G pH 7.5, containing radiolabelled substrates (150 µM L-[U-^{14}C]leucine) and inhibitors as indicated in the figures or table, in a 37 °C water bath for 6 minutes. To terminate transport, cells were washed three times with ice-cold HBSS pH 7.5. For measuring sodium-independent uptake, NaCl in HBSS + G was replaced by NMDG-Cl and Na^+-salts were replaced by K^+-salts. Cells were then harvested by homogenizing with 500 µl of 0.1 M HCl. An aliquot of 400 µl was used for scintillation counting and the remainder for protein quantification using Bradford reagent.

Statistics

All data points in figures and tables were taken from distinct samples with (n) giving the number of biologically unique samples measured.

Reporting summary

Further information on research design is available in the Nature Portfolio Reporting Summary linked to this article.

Data availability

The data that support this study are available from the corresponding authors upon request. The cryo-EM maps have been deposited in the Electron Microscopy Data Bank (EMDB) under accession codes EMD-37427 (Cryo-EM map of ACE2-B^{0}AT1 complex with JX98); EMD-37428 (Cryo-EM map of ACE2-B^{0}AT1 complex with JX225); the atomic coordinates have been deposited in the Protein Data Bank (PDB) under accession codes 8WBY (Cryo-EM structure of ACE2-B^{0}AT1 complex with JX98); and 8WBZ (Cryo-EM structure of ACE2-B^{0}AT1 complex with JX225). The X-ray crystal structure of JX98 and JX225 were deposited in the Cambridge Crystallographic Data Centre (CCDC-2300201 and CCDC-2300200). The source data underlying Figs. 1, 2, 3 and Supplementary Table 1 and Figure S1 are provided as a Source Data file associated with this publication. Source data are provided with this paper.

References

1. Broer, S. & Gauthier-Coles, G. Amino acid homeostasis in mammalian cells with a focus on amino acid transport. *J. Nutr.* **152**, 16–28 (2022).
2. Blau, N., Duran, M., Gibson, K. M. & Dionisi-Vici, C. *Physician's guide to the diagnosis, treatment, and follow-up of inherited metabolic disease*. 3-141 (Springer-Verlag, 2014).

3. Holecek, M. Why are branched-chain amino acids increased in starvation and diabetes? *Nutrients* **12**, 3087 (2020).
4. White, P. J. et al. Insulin action, type 2 diabetes, and branched-chain amino acids: A two-way street. *Mol. Metab.* 101261 https://doi.org/10.1016/j.molmet.2021.101261 (2021).
5. Palacin, M. & Broer, S. in *Physician's Guide to the Diagnosis, Treatment, and Follow-Up of Inherited Metabolic* Diseases (eds B. Thöny, M. Duran, K. M. Gibson, & C. Dionisi-Vici) 85-99 (Springer-Verlag, 2014).
6. Seow, H. F. et al. Hartnup disorder is caused by mutations in the gene encoding the neutral amino acid transporter SLC6A19. *Nat. Genet* **36**, 1003–1007 (2004).
7. Belanger, A. M. et al. Inhibiting neutral amino acid transport for the treatment of phenylketonuria. *JCI Insight* **3**, e121762 (2018).
8. Belanger, A. J. et al. Excretion of excess nitrogen and increased survival by loss of SLC6A19 in a mouse model of ornithine transcarbamylase deficiency. *Journal of Inherited Metabolic Disease* **n/a** https://doi.org/10.1002/jimd.12568 (2022).
9. Jiang, Y. et al. Mice lacking neutral amino acid transporter B(0)AT1 (Slc6a19) have elevated levels of FGF21 and GLP-1 and improved glycaemic control. *Mol. Metab.* **4**, 406–417 (2015).
10. Yadav, A. et al. Novel chemical scaffolds to inhibit the neutral amino acid transporter B(0)AT1 (SLC6A19), a potential target to treat metabolic diseases. *Front. Pharm.* **11**, 140 (2020).
11. Navarro-Garrido, A. et al. Aristolochic acid-induced nephropathy is attenuated in mice lacking the neutral amino acid transporter B(0) AT1 (Slc6a19). *Am. J. Physiol. Renal Physiol.* https://doi.org/10.1152/ajprenal.00181.2022 (2022).
12. Pochini, L. et al. Nimesulide binding site in the B0AT1 (SLC6A19) amino acid transporter. Mechanism of inhibition revealed by proteoliposome transport assay and molecular modelling. *Biochem Pharm.* **89**, 422–430 (2014).
13. Desai, J. et al. Discovery of novel, potent and orally efficacious inhibitor of neutral amino acid transporter B(0)AT1 (SLC6A19). *Bioorg. Med Chem. Lett.* **53**, 128421 (2021).
14. Cheng, Q. et al. Identification of novel inhibitors of the amino acid transporter B(0) AT1 (SLC6A19), a potential target to induce protein restriction and to treat type 2 diabetes. *Br. J. Pharm.* **174**, 468–482 (2017).
15. Danthi, S. J. et al. Identification and characterization of inhibitors of a neutral amino acid transporter, SLC6A19, using two functional cell-based assays. *SLAS Discov.* 2472555218794627 https://doi.org/10.1177/2472555218794627 (2018).
16. Gerbeth-Kreul, C. et al. A solid supported membrane-based technology for electrophysical screening of B(0)AT1-modulating compounds. *SLAS Discov.* **26**, 783–797 (2021).
17. Broer, S. & Gether, U. The solute carrier 6 family of transporters. *Br. J. Pharm.* **167**, 256–278 (2012).
18. Danilczyk, U. et al. Essential role for collectrin in renal amino acid transport. *Nature* **444**, 1088–1091 (2006).
19. Kowalczuk, S. et al. A protein complex in the brush-border membrane explains a Hartnup disorder allele. *FASEB J.* **22**, 2880–2887 (2008).
20. Yan, R. et al. Structural basis for the recognition of SARS-CoV-2 by full-length human ACE2. *Science* **367**, 1444–1448 (2020).
21. Shi, L., Quick, M., Zhao, Y., Weinstein, H. & Javitch, J. A. The mechanism of a neurotransmitter:sodium symporter-inward release of Na+ and substrate is triggered by substrate in a second binding site. *Mol. Cell* **30**, 667–677 (2008).
22. Navratna, V. & Gouaux, E. Insights into the mechanism and pharmacology of neurotransmitter sodium symporters. *Curr. Opin. Struct. Biol.* **54**, 161–170 (2019).
23. Cheng, M. H. & Bahar, I. Monoamine transporters: structure, intrinsic dynamics and allosteric regulation. *Nat. Struct. Mol. Biol.* **26**, 545–556 (2019).
24. Niello, M., Gradisch, R., Loland, C. J., Stockner, T. & Sitte, H. H. Allosteric modulation of neurotransmitter transporters as a therapeutic strategy. *Trends Pharm. Sci.* **41**, 446–463 (2020).
25. Shotwell, M. A., Jayme, D. W., Kilberg, M. S. & Oxender, D. L. Neutral amino acid transport systems in Chinese hamster ovary cells. *J. Biol. Chem.* **256**, 5422–5427 (1981).
26. Broer, S. & Broer, A. Amino acid homeostasis and signalling in mammalian cells and organisms. *Biochem J.* **474**, 1935–1963 (2017).
27. Fairweather, S. J. et al. A GC-MS/single-cell method to evaluate membrane transporter substrate specificity and signaling. *Front Mol. Biosci.* **8**, 646574 (2021).
28. Gauthier-Coles, G. et al. Quantitative modelling of amino acid transport and homeostasis in mammalian cells. *Nat. Commun.* **12**, 5282 (2021).
29. Wempe, M. F. et al. Metabolism and pharmacokinetic studies of JPH203, an L-amino acid transporter 1 (LAT1) selective compound. *Drug Metab. Pharmacokinet.* **27**, 155–161 (2012).
30. Esslinger, C. S., Cybulski, K. A. & Rhoderick, J. F. Ngamma-aryl glutamine analogues as probes of the ASCT2 neutral amino acid transporter binding site. *Bioorg. Med Chem.* **13**, 1111–1118 (2005).
31. Kuhn, B., Mohr, P. & Stahl, M. Intramolecular hydrogen bonding in medicinal chemistry. *J. Med Chem.* **53**, 2601–2611 (2010).
32. Cavallo, G. et al. The Halogen Bond. *Chem. Rev.* **116**, 2478–2601 (2016).
33. Cinčić, D., Friščić, T. & Jones, W. Isostructural materials achieved by using structurally equivalent donors and acceptors in halogen-bonded cocrystals. *Chem. – A Eur. J.* **14**, 747–753 (2008).
34. Shen, Y. et al. Structures of ACE2-SIT1 recognized by Omicron variants of SARS-CoV-2. *Cell Discov.* **8**, 123 (2022).
35. Wobst, H. et al. A small molecule slc6a19 inhibitor increases urinary phenylalanine excretion and reduces its pathogenic plasma accumulation in a phenylketonuria mouse model. *Mol. Genet. Metab.* **138**, 107502 (2023).
36. Silbernagl, S. Cycloleucine (1-amino-cyclopentane carboxylic acid): tubular reabsorption and inhibitory effect on amino acid transport in the rat kidney. (Microperfusion experiments). *Pflug. Arch.* **353**, 241–253 (1975).
37. Wilensky, A. J., Lane, E. A., Levy, R. H., Ojemann, L. M. & Friel, P. N. Differential kinetics of cinromide and two of its metabolites in epileptic patients. *Eur. J. Clin. Pharm.* **21**, 149–153 (1981).
38. Coleman, J. A. & Gouaux, E. Structural basis for recognition of diverse antidepressants by the human serotonin transporter. *Nat. Struct. Mol. Biol.* **25**, 170–175 (2018).
39. Plenge, P. et al. The mechanism of a high-affinity allosteric inhibitor of the serotonin transporter. *Nat. Commun.* **11**, 1491 (2020).
40. Quick, M. et al. The LeuT-fold neurotransmitter:sodium symporter MhsT has two substrate sites. *Proc. Natl Acad. Sci. USA* **115**, E7924–E7931 (2018).
41. Li, Y. et al. Structural insight into the substrate recognition and transport mechanism of amino acid transporter complex ACE2-B(0) AT1 and ACE2-SIT1. *Cell Discov.* **9**, 93 (2023).
42. Zhang, K. Gctf: Real-time CTF determination and correction. *J. Struct. Biol.* **193**, 1–12 (2016).
43. Zivanov, J. et al. New tools for automated high-resolution cryo-EM structure determination in RELION-3. *Elife* **7**, e42166 (2018).
44. Kimanius, D., Forsberg, B. O., Scheres, S. H. & Lindahl, E. Accelerated cryo-EM structure determination with parallelisation using GPUs in RELION-2. *Elife* **5**, e18722 (2016).
45. Scheres, S. H. RELION: implementation of a Bayesian approach to cryo-EM structure determination. *J. Struct. Biol.* **180**, 519–530 (2012).
46. Scheres, S. H. A Bayesian view on cryo-EM structure determination. *J. Mol. Biol.* **415**, 406–418 (2012).

47. Punjani, A., Rubinstein, J. L., Fleet, D. J. & Brubaker, M. A. cryoSPARC: algorithms for rapid unsupervised cryo-EM structure determination. *Nat. Methods* **14**, 290–296 (2017).
48. Rosenthal, P. B. & Henderson, R. Optimal determination of particle orientation, absolute hand, and contrast loss in single-particle electron cryomicroscopy. *J. Mol. Biol.* **333**, 721–745 (2003).
49. Emsley, P., Lohkamp, B., Scott, W. G. & Cowtan, K. Features and development of Coot. *Acta Crystallogr. Sect. D., Biol. Crystallogr.* **66**, 486–501 (2010).
50. Adams, P. D. et al. PHENIX: a comprehensive Python-based system for macromolecular structure solution. *Acta Crystallogr. Sect. D., Biol. Crystallogr.* **66**, 213–221 (2010).

Acknowledgements

The authors thank Jędrzej Kukułowicz for helping with modelling inhibitor binding to B^0AT1. We also thank the Cryo-EM Facility of Southern University of Science and Technology (SUSTech) for providing the facility support. We thank Shuman Xu and Lei Zhang at the Cryo-EM Center of SUSTech for technical support in electron microscopy data acquisition. This work was funded by the Shenzhen Medical Research Fund (A2303046 to R.Y.) and by NHMRC grant GNT2020757 to S.B.

Author contributions

J.X. performed medicinal chemistry; Z.H., L.D. and M.G.G. performed structural biology experiments, A.Y., Y.J. and A.B. performed pharmacological experiments, all authors analyzed data and prepared data for publication, M.M., R.Y., and S.B. conceived the study, wrote the manuscript, and compiled data for publication. All authors edited the manuscript.

Competing interests

The authors declare no competing interests.

Additional information

Supplementary information The online version contains supplementary material available at https://doi.org/10.1038/s41467-024-51748-1.

Correspondence and requests for materials should be addressed to Renhong Yan or Stefan Bröer.

Peer review information *Nature Communications* thanks Natasha Freidman, Dmitry Semchonok, and the other, anonymous, reviewer(s) for their contribution to the peer review of this work. A peer review file is available.